Pressure-induced structure, elasticity, intrinsic hardness and ideal strength of tetragonal C4N†

Zhijun Shi,[ab] Wei Shao,[a] Lixiang Rao,[a] Xiaolei Xing,[c] Yefei Zhou,[c] Xuejun Ren[d] and

Qingxiang Yang *[a]

[a] State Key Laboratory of Metastable Materials Science & Technology, Yanshan University, Qinhuangdao 066004, P. R. China. E-mail: qxyang@ysu.edu.cn; Tel: +86 18633515955
[b] State Key Laboratory of Tribology, Tsinghua University, Beijing 100084, P. R. China
[c] College of Mechanical Engineering, Yanshan University, Qinhuangdao 066004, P. R. China
[d] School of Engineering, Liverpool John Moores University, Liverpool L3 3AF, UK

A tetragonal C4N (t-C4N) structure was predicted via CALYPSO code, and the effects of pressure on its structural and mechanical properties were studied. The results show that t-C4N is different from various 2D CxNy compounds with a new type 3D crystal structure, which is similar to diamond. Bulk t-C4N is equipped with excellent elastic properties. When the pressure is increased from 0 GPa to 350 GPa, its bulk modulus B, shear modulus G and Young's modulus E are increased from 426.9 GPa to 1123.1 GPa, 371.4 GPa to 582.9 GPa and 863.7 GPa to 1490.9 GPa, respectively. The anisotropic Bmax, Gmax and Emax are increased from 582.38 GPa to 1751.41 GPa, 478.29 GPa to 1033.97 GPa and 1281.26 GPa to 2490.14 GPa, respectively. When the pressure is 0 GPa, the hardness calculated by Chen's and Tian's models are 51.15 GPa and 51.81 GPa, respectively. Its ideal tensile strength in [111] orientation is the smallest (63.46 GPa), which indicates that the (111) planes allow easy cleavage. The smallest ideal shear strength (67.98 GPa) can be obtained in the (111)[1% 10] orientation, which suggests its theoretical hardness is about 67.98 GPa. Due to its excellent mechanical properties, t-C4N can be used as an industrial superhard material.

I. Introduction

Carbon materials such as diamond,[1] graphene[2] and its allotropes[3,4] have attracted extensive attention because of their advantages such as high chemical stability, high electrical conductivity and excellent mechanical properties.[5] Nevertheless, the performance of pure carbon materials is largely limited by the intrinsic properties of carbon atoms. It has been found that the introduction of second type atoms, through heteroatom doping for example,[6] is one of the most effective strategies for tailoring the structure and properties of pure carbon materials.[7] Among a variety of binary synthetic carbon materials, carbonitrides are the most familiar and commonly used, and a lot of studies have been devoted to exploring and revealing the unknown physical chemical properties and mechanisms of carbonitrides such as CN,[8] C2N,[9] C3N,[10] C3N2, [11] C4N[12] and C3N4.[13]

At present, most of the research studies are focused on two-dimensional (2D) carbonitrides, which are generally equipped with excellent optical, electrical and catalytic properties. The graphite-like carbonitride (g-C3N4) has been investigated for a long time,[14] which can be applied in energy sources and environmental fields like hydrogen manufacturing,[15] efficient energy storage[16] and photocatalytic degradation of pollutants.[17] With a large adjustable band gap and superior symmetry, 2D C2N has many potential applications in electronic and optoelectronic devices.[18,19] C3N is a 2D carbon-based semiconductor with an adjustable indirect band gap and excellent mechanical properties.[20] These interesting physical characteristics of C3N lead to a great potential for practical application in the future electronics industry field.[21]

In recent years, as a member of the carbonitride family, C4N with a stoichiometric ratio of C/N = 4 : 1 has been increasingly investigated and reported. Li et al.[22] proposed two new single-layered C4N with dumbbell structures and found that their high Fermi speeds make them potentially ideal materials for high-speed electronic devices. Zhang et al.[23] revealed that 2D C4N layers with hexagonal holes show an ordered crystal structure and good electro-catalytic performance. Yang et al.[24] successfully synthesized a novel 2D semiconductor covalent organic framework C4N (C4N-COF) with a direct band gap via a hydrothermal solvent method. Wang et al.[25] designed and predicted its new crystal structures via crystal structure analysis using CALYPSO (Crystal structure AnaLYsis by Particle Swarm Optimization) code with a global structure search method. Pu et al.[26] designed a graphite–carbon nitride C4N nanosheet using CALYPSO code and found that it is thermodynamically stable via theoretical calculation. Although it has great potential for photoelectric and catalytic applications, the mechanical properties of 2D carbonitride are a disadvantage compared with that of bulk materials. Common superhard materials usually have three-dimensional (3D) bulk crystal structures, such as BC3, [27] FeB4, [28] B3N5, [29] c-BN[30] and t-BN.[31] These materials with excellent mechanical properties have a common characteristic, that is, they are all 3D and densely packed bulk structures consisting of strongly covalent bonding networks.[32] It is very significant and urgent to investigate the mechanical properties of bulk C4N from the perspectives of both fundamental science and future engineering applications. However, there are few reports on the design, preparation and relevant mechanical properties of bulk C4N.

Pressure is a fundamental thermodynamic variable, which can be used to control the properties of materials by reducing interatomic distances, modifying electronic orbitals and bonding characteristics.[32] Actually, many new carbonitrides that can be used as superhard materials have been discovered under high pressure,[33] such as CN2 (HV = 70 GPa),[32] C3N2 (HV = 86 Gpa)[32] and C3N4 (HV = 92 Gpa).[34] Therefore, pressure-induced elasticity, hardness and ideal strength of t-C4N are things worth investigating.

Many successful examples have proved that first principles structure prediction can reliably search for unknown structures.[29] Lu et al.[35]investigated diamond (100) surfaces using the structure swarm intelligence automatic surface structure exploration method, which reveals an unexpected surface reconstruction featuring self-assembled carbon nanotube arrays. Gao et al.[36] proposed an effffective method for interface structure prediction by generalizing the CALYPSO method and predicting two unknown grain boundary (GB) structures of rutile TiO2 using this method. Yin et al.[37] developed a convenient and reliable method for solving transition state location problems, and they successfully located the minimum energy path (MEP) of direct low temperature pressure induced phase transition for FCC silicon to a simple hexagonal phase and FCC lithium to a complex body-centered cubic cl16 high pressure phase.

In this work, CALYPSO code was performed to design and predict 3D carbonitride with a stoichiometric ratio C/N = 4 : 1. The thermodynamics stability of tetragonal C4N (t-C4N) was calculated using a first principles method. Its electrical property and bond characteristics were analyzed using the band structure and density of states (DOS). Under the effects of incremental applied pressure, the structural parameters, elastic moduli and intrinsic hardness of bulk t-C4N were studied, and the effects of pressure on the mechanical properties and anisotropy were analyzed. The ideal tensile strengths of the different crystal faces were calculated to reveal the weak planes allowing easy cleavage, and the minimum ideal shear strength of the weak plane was used to obtain the accurate theoretical hardness of t-C4N. This can provide theoretical guidance for the design of bulk C4N and help to understand the effect of pressure on its mechanical properties.

II. Computational details

All first principles calculations were performed using the Vienna Ab-initio Simulation Package (VASP).[38] Pseudopotentials utilized to describe the reactions between the atomic nuclei and valence electrons were obtained using a projector augmented wave method.[39] In the energy, elastic properties and electronic structure calculations, the Generalized Gradient Approximation[40] exchange correlation functional modified by Perdew, Burke and Ernzerhof (GGA-PBE) was applied, which takes the electron density nonuniformity into account. However, the GGA method usually overestimates the lattice constants, and Local Density Approximation (LDA)41 was used as the exchange correlation functional in the tensile and shear calculations. On the basis of convergence tests (Fig. S1, ESI†), the cutoffff energy value of the plane wave was set as 800 eV and K points constructed using the Monkhorst–Pack scheme[42] in the Brillouin area was set as 8 x 8 x 8. The finite displacement method and a 2 x 2 x 2 supercell was used for phonon dispersion spectrum calculation.[43,44] When the energy change between two relaxation steps is less than 1.0x 10^{-5} eV and the absolute value of ionic force change is less than 1.0 x10^{-3} eV $Å^{-1}$, the crystal structure optimization can be determined to achieve the desired accuracy. The spin-polarized (ISPIN = 2) density of states (DOS) was calculated and the symmetric DOS (Fig. S2, ESI†) indicates that the t-C4N structure is not magnetic. Thus spin polarization was not considered in this work. The pressure applied by the input file parameter PSTRESS was hydrostatic pressure from 0 GPa to 350 GPa (3500 kbar). The maximum pressure that could be applied in the normal calculation process was 350 GPa, as a higher pressure could lead to interruption with unknown errors. The elastic constants of t-C4N were calculated using a well-developed strain–energy method.4,45 The ideal tensile/shear strength was calculated using an ideal-strength-VASP method.46,47 Strain energy–strain relationship can be obtained with fixed X-axis optimization with a 1% strain step after VASP code modification. After a series of energy calculations, the uniaxial tensile stress s and shear stress t can be calculated by the following equations:47

$$\sigma = \frac{(1+\varepsilon)}{V(\varepsilon)}\frac{\partial E}{\partial \varepsilon} \qquad (1)$$

$$\tau = \frac{1}{V(\varepsilon)}\frac{\partial E}{\partial \varepsilon} \qquad (2)$$

where, E is the strain energy of the system corresponding to the tensile strain ε at each step and V(ε) is the structural volume under the corresponding strain.

By combining the energy–strain relationship with V(ε) and eqn (1) and (2), the stress–strain curves in tensile/shear orientations were obtained. In the C4N crystal prediction via CALYPSO code,36 we defined the numbers of atoms for each chemical species in one formula unit to be 4 for C and 1 for N. The maximum number of formula units per cell is 2. The primary estimated volume per formula unit is 21 Å^3 . The local PSO algorithm was adopted in the simulation, and it is interfaced with VASP as a local optimization method. The proportion of the structures generated by PSO is 60% and the rest of structures will then be randomly generated with symmetry constraints. The population size of the predicted structures is 40 in every generation. The Max step for generations is set to 50.

III. Results and discussion

Crystal structure and stability of t-C4N Schematic diagrams of the crystal structures used in the following calculations are shown in Fig. 1. Fig. 1(a) is the unit cell of t-C4N (which belongs to the tetragonal system) obtained by the CALYPSO method, and Fig. S3 (ESI†) is its calculated X-ray diffraction (XRD) spectrum. The brown spheres represent C atoms and the pale lilac ones represent N atoms. Its optimized lattice constants are a = b = 3.47 Å and c = 4.85 Å. Fig. 1(b) is the single unit cell of diamond. It can be found that t-C4N has a diamond-like structure. The diamond structure belongs to the $Fd\bar{3}m$ space group and all C atoms are located at 8a Wyckoff sites (Table S1, ESI†). However, the t-C4N structure belongs to the $P\bar{4}2_1m$ space group. In a t-C4N conventional cell, two N atoms and two C atoms are located at 2c Wyckoff sites, and the other C atoms are located at 2a and 4e Wyckoff sites, respectively (Table S2, ESI†). A crystal structure similar to t-C4N can be formed by replacing 4 C–C bonds in the diamond structure with 4 N atoms and 8 C–N bonds at 2c Wyckoff sites. The difference between t-C4N and the diamond is the changes in bond lengths and bond angles (listed in Tables S3–S5, ESI†). The bond length of the C–C covalent bonds in diamond is 1.54 Å. Its bond angle is 109.471 for C–C–C and the dihedral angles are 601/1801 for C–C–C–C. There are two types of C–N bonds in t-C4N, in which, the bond length of the ones parallel to the Z-axis is 1.38 Å, and that of the other ones is 1.48 Å with an 123.781 angle with the Z-axis. The lengths of the two types of C–C bonds in t-C4N are 1.51 A and 1.55 A, respectively. There are 9 kinds of different bond angles distributed from 106.911 to 123.831 in t-C4N (Table S4, ESI†), and 15 kinds of different dihedral angles ranging from 58.251 to 1801 (Table S5, ESI†).

In order to investigate the thermodynamics stability of t-C4N, the formation energy and phonon spectrum were calculated. The formation energy48 is defined as:

$$E_{\mathrm{f}}(\mathrm{C}_x\mathrm{N}_{1-x}) = E_{\mathrm{coh}}(\mathrm{C}_x\mathrm{N}_{1-x}) - x\mu_{\mathrm{C}} - (1-x)\mu_{\mathrm{N}} \qquad (3)$$

where, Ecoh(CxN1_x) represents the cohesive energy of the CxN1_x compound (in eV per atom), and the chemical potentials of C (μ_C) and N (μ_N) can be obtained from the cohesive energy of graphite and molecular N2, respectively.

Cohesive energy (Ecoh) is defined as the difference between the energy of the compounds and the total energy of the corresponding isolated atoms[49] and the equation is as follows:

$$E_{\mathrm{coh}} = (E_{\mathrm{bulk}} - mE_{\mathrm{C}} - nE_{\mathrm{N}})/(m + n) \qquad (4)$$

where Ebulk is the total energy of the bulk structure, EC and EN are the energies of the isolated C atom and N atom in a vacuum, respectively, and m and n represent the number of C atoms and N atoms.

The calculated Ecoh of bulk t-C4N is -8.44 eV, which indicates that it is an exothermic process when isolated C and N atoms form condensed matter C4N. Those of graphite and molecular N2 are -9.23 eV and -6.37 eV, respectively. The calculated formation energy of t-C4N is 0.22 eV, which is lower than the computational ones of C4N (0.97 eV), experimentally available C2N (0.95 eV) and C3N4 (0.96 eV).[50] Therefore, we believe that t-C4N is thermodynamically stable and it can be synthesized through experiment or industry.

The thermodynamic stability and bulk properties of t-C4N are shown in Fig. 2. Fig. 2(a) is the phonon spectrum, and the absence of imaginary frequency proves its thermodynamic stability. Fig. 2(b) is the band structure of t-C4N, where the dashed line represents the location of the Fermi level. There are bands across the Fermi level, which indicate the system exhibits some metallic characteristics. The bands passing through the Fermi level are valence bands, which indicate the electric conduction phenomena of the valence bands in t-C4N, and the band gap of the forbidden band limits its conductivity to some extent. Fig. 2(c) is the total density of states (TDOS) and the partial density of states (PDOS) corresponding to the band structure, where the dashed line represents the location of the Fermi level. There are PDOS peaks of C and N atoms at the Fermi level, and both of them contribute to the metallic properties. The PDOS peak shape and intensity of C-p and N-p orbitals in the range from -3.5 eV to -2.0 eV are similar. Those of N-p and C_{34}-p orbitals in the range from -4.5 eV to -3.5 eV are basically similar. Their orbital hybridization and interaction contribute to the covalent bond formation. Therefore, the bond type of bulk t-C4N is a mixture of covalent bonds and metallic ones.
In addition, an ab-initio molecular dynamics (AIMD) simulation was performed via VASP to validate the stability of the structures at room temperature.[51,52] Fig. 3 shows the relationship between total energy and simulation time, as well as the changes in the t-C4N structure. There are 216 C atoms and 54 N atoms in the t-C4N supercell. After 9 ps relaxation at 300 K (NVT ensemble), there are some atomic displacements. But the change in overall structure is small. The energy fluctuation is relatively stable with an amplitude of about 5 eV. This indicates that the t-C4N structure is thermodynamically stable at 300 K.

B. Effects of pressure on the crystal structure and elastic constants of t-C4N The pressure-induced changes in the lattice constants and unit cell volume of t-C4N are shown in Fig. 4 (detailed data are listed in Table S6, ESI†). The a/a0, c/c0 and V/V0 ratios are all gradually decreased with the increase of pressure. Under a certain pressure, a/a0 is always lower than c/c0. It can be inferred that t-C4N is compressed along the a-axis more easily than along the c-axis, that is, the c-axis is less sensitive to external pressure. This is also evidenced by the gradually increased c/a ratio listed in Table S6 (ESI†). In addition, when the pressure is increased from 0 GPa to 350 GPa, the cell type (tetragonal) and space group $(P\bar{4}2_1m)$ remain unchanged. The only change occurs in the lattice parameter of t-C4N. To study the stability of the t-C4N structure under different pressures, the enthalpy of t-C4N, diamond, graphite and two 2D C4N50 are calculated and the changes of their enthalpies under different pressures relative to that of graphite are shown in Fig. 5. It can be seen that t-C4N is more stable than the 2D C4N structures under pressure. The stability of diamond is better than that of t-C4N, and their enthalpy changes have similar trends. When the pressure is higher than 150 GPa, t-C4N becomes more stable than graphite. Therefore, it is promising that t-C4N can be synthesized experimentally using suitable precursors under high pressure.

The bulk t-C4N structure is similar to a diamond-like structure to some extent, and its mechanical properties are worthy of attention and further study. The intrinsic mechanical properties of materials can be characterized by a complete set of single crystal elastic constants (Cij) and typical polycrystalline moduli.[53] For the tetragonal system, the single crystal elastic constants C11, C12, C13, C33,C44 and C66 can be obtained by an energy–strain relationship. The results of the calculated elastic constants Cij of t-C4N are listed in Table 1. They all satisfy the Born–Huang tetragonal lattice stability requirements54 listed as follows:

$$C_{11} > 0;\ C_{33} > 0;\ C_{44} > 0;\ C_{66} > 0;\ C_{11}-C_{12} > 0;\ (C_{11} + C_{33}- 2C_{13}) > 0;\ [2(C_{11}-C_{12}) + C_{33} + 4C_{13}] > 0 \qquad (5)$$

The changing curves of the pressure-induced elastic constants and stiffness constants are shown in Fig. 6. In Fig. 6(a), the elastic constants Cij are increased with the increase of pressure. At a certain pressure, C33 is the largest in all the elastic constants and its increase rate (slope of curve) is also the greatest. C44 is the smallest in all the elastic constants. The curve change trends of C11, C12 and C13 are basically the same, and they always meet the law of C11 4 C12 4 C13. When the pressure is 0 GPa, C44 is close to C66 and they are larger than C12 and C13. However, C44 is surpassed by C12 when the pressure is increased to 100 GPa, and it is surpassed by C13 when the pressure is further increased to 300 GPa. With the increase of pressure, the difference between C12 and C66 is decreased gradually, and that between C44 and C66 is increased. In Fig. 6(b), the stiffness constant ratio of the cubic crystal system C33/C11 = C13/C12 = C66/C44 = 1 is represented by the green dashed line. It is obvious that the stiffness constant ratios C33/C11, C13/C12 and C66/C44 of t-C4N exhibit unique pseudoelastic behaviors. When the pressure is increased from 0 GPa to 350 GPa, C33/C11 and C13/C12 vary slightly around 1.85 and 0.55, respectively. C66/C44 has a wide variation range, and is increased from 1.06 at 0 GPa to 1.85 at 350 GPa. It is also revealed that the pressure-induced elastic properties of the single cell t-C4N crystal structure have a strong orientation effect.

Based on its Cij matrix, polycrystalline bulk modulus B (BV, BR) and shear modulus G (GV, GR) can be calculated using Voigt[55] and Reuss[56] methods. Hill[57] proved through the extremum principle that the calculated results of the Voigt and Reuss models were the upper and lower limits of elastic moduli, respectively. Their arithmetic mean values (BH, GH) are closer to the experimental results, which are usually used to represent the polycrystalline elastic moduli. The equations of elastic moduli based on the VRH (Voigt–Reuss–Hill) method[55–57] are shown as follows:

$$B_V = [2(C_{11} + C_{12}) + 4C_{13} + C_{33}]/9 \qquad (6)$$

$$G_V = (M + 3C_{11} - 3C_{12} + 12C_{44} + 6C_{66})/30 \qquad (7)$$

$$B_R = C^2/M \qquad (8)$$

$$G_R = 15\{18(B_V/C^2) + [6/(C_{11}-C_{12})] + (6/C_{44}) + (3/C_{66})\}^{-1} \qquad (9)$$

$$M = C_{11} + C_{12} + 2C_{33} - 4C_{13},\ C^2 = (C_{11} + C_{12})C_{33} - 2C_{13}{}^2 \qquad (10)$$

$$B_H = (B_V + B_R)/2 \qquad (11)$$

$$G_H = (G_V + G_R)/2 \qquad (12)$$

Based on the calculated results of B and G, Young's modulus E58 can be calculated via the following equation:

$$E_{VRH} = 9B_{VRH}G_{VRH}/(3B_{VRH} + G_{VRH}) \qquad (13)$$

The calculated B, G and E under different pressures are listed in Table 2, and the curves of pressure-induced B, G and E are shown in Fig. 7. With the increase of pressure, B is mainly increased linearly. The major influence on E is contributed by G and their increase rates reduce with the increase of pressure. When the pressure is 0 GPa, polycrystalline BH, GH and EH of t-C4N are 426.9 GPa, 371.4 GPa and 863.7 GPa, respectively. When the pressure is increased to 50 GPa, its BH, GH and EH are improved to 553.9

GPa, 424.6 GPa and 1014.5 GPa, respectively. Their increase rates are 29.7%, 14.3% and 17.4%, respectively, which are the most sloping parts in the elastic moduli–pressure curves. Then, the slopes of the pressure-induced elastic moduli curves are gradually decreased with the increase of pressure. When the pressure is increased to 300 GPa, the polycrystalline BH, GH and EH of t-C4N are 1053.5 GPa, 570.3 GPa and 1449.4 GPa, respectively. When the pressure is increased to 350 GPa, its BH, GH and EH are further improved to 1123.1 GPa, 582.9 GPa and 1490.9 GPa, respectively. Their increase rates are 6.6%, 2.2% and 2.8%, which are the least sloping parts in the elastic moduli–pressure curves. It should be noticed that the difference between the upper and lower limits of the elastic moduli of the t-C4N crystal structure, calculated using the Voigt and Reuss method, is gradually increased with the increase of pressure, which indicates that the anisotropy of the elastic moduli are inevitably improved with the increase of pressure.

C. Anisotropic elastic moduli of t-C4N The pressure-induced anisotropic elastic moduli B, G, E and their 3D surface constructions were obtained using the Cij matrix and post-processing software.[59,60] The minimum (Bmin), maximum (Bmax) and 3D surface constructions of pressure induced bulk moduli (B) are shown in Fig. 8. Bmin and Bmax are both increased with the increase of pressure. The increase in the maximum value is steeper than that of the minimum value, and the difference between them increases the anisotropy of the bulk modulus, which can also be known from the pressure-induced change of its 3D surface constructions. In the 3D surface constructions of B, the blue areas represent the locations of Bmin and the yellow ones represent those of Bmax. With the increase of pressure, it can be clearly observed that the ellipsoid 3D surface constructions of B become longer along the [001] direction, which intuitively indicates the increase in anisotropy of B. The detailed data of Bmin and Bmax under different pressure are listed in Table S7 (ESI†). When the pressure is 0 GPa, the values of Bmin and Bmax are 368.85 GPa and 582.38 GPa, respectively. When the pressure is increased to 350 GPa, the values of Bmin and Bmax are increased to 929.74 GPa and 1751.41 GPa, respectively. The anisotropy of B is increased from 1.58 to 1.88 when the pressure is increased from 0 GPa to 350 GPa.

The minimum (Gmin), maximum (Gmax) and 3D surface constructions of pressure-induced shear moduli (G) are shown in Fig. 9. It can be obviously observed that Gmax is increased with the increase in pressure, and a steeper increase occurs when the pressure is above 250 GPa. If 250 GPa is taken as the dividing line, Gmin presents opposite increasing or decreasing trends and its changes are relatively small. The different pressure-induced behaviors between Gmin and Gmax lead to a dramatic increase in anisotropy, which can also be revealed by changes of 3D surface constructions with different pressures. In the 3D surface constructions of G, the blue areas represent the locations of Gmin and the yellow ones represent those of Gmax. The area expansion of the blue region and a more angular surface construction of G appear with the increase in pressure, which suggests an increase in the anisotropy of G. The detailed data of Gmin and Gmax under different pressure are listed in Table S7 (ESI†). When the pressure is 0 GPa, the values of Gmin and Gmax are 215.02 GPa and 478.29 GPa, respectively. When the pressure is increased to 350 GPa, the values of Gmin and Gmax are increased to 235.73 GPa and 1033.97 GPa, respectively. The anisotropy of G is increased from 2.22 to 4.39 when the pressure is increased from 0 GPa to 350 GPa.

The minimum (Emin), maximum (Emax) and 3D surface constructions of pressure-induced Young's moduli (E) are shown in Fig. 10. From Fig. 10, both Emin and Emax are increased with the increase of pressure, except for a slight drop in Emin at 350 GPa. The increase rate of Emax is much larger than that of Emin, which can lead to the increase in anisotropy of E. In the 3D surface constructions of E, the blue areas represent the relatively smaller values of E and the yellow areas represent the larger ones. The blue areas always appear in the [100] and [010] orientations, and the large yellow areas appear in the [001] orientation. It is worth noting that with the increase of pressure, the yellow region with a larger E value also gradually appeared in the [110] orientation. Nevertheless, the projection analysis of different planes is needed to reveal the locations of the Emin and Emax values. The detailed data of Emin and Emax with different pressures are listed in Table S7 (ESI†). When the pressure is 0 GPa, the values of Emin and Emax are 599.98 GPa and 1281.26 GPa, respectively. When the pressure is increased to 350

GPa, the values of Emin and Emax are increased to 773.50 GPa and 2490.14 GPa, respectively. The anisotropy of E is increased from 2.14 to 3.22 when the pressure is increased from 0 GPa to 350 GPa.

The projections of the (001) and (010) planes in the 3D surface constructions of B, G and E are shown in Fig. 11 (only one quarter of the projection is given based on symmetry). According to line spacing with different pressures in the projections, the change rates of elastic moduli B, G and E are decreased with the increase of pressure.

In addition, the change rates of partial B, G and E are increased abnormally with the increase of pressure from 250 GPa to 300 GPa. In Fig. 11(a), the (001) projections of B are approximately perfect circles. Bmin can be obtained in any orientation of these circles including [100], [010], and [110]. In Fig. 11(b), the (010) projections of B are ellipses with long axis along the [001] orientation, where Bmax can be obtained. In Fig. 11(c), the (001) projections of G are quadrangles with concave hypotenuses. Gmin can be obtained in [110] orientation. In Fig. 11(d), the (010) projections of G are ellipses with a long axis along the [100] orientation. Combined with the projection results of the (001) planes, Gmax can be obtained in both [100] and [010] orientations. In Fig. 11(e), the (001) projections of E are four-sided stars with angles along the [110] orientation. Emin can be obtained in both [100] and [010] orientations. In Fig. 11(f), the (010) projections of E are approximately spindles. Emax can be obtained in the [001] orientations. Especially, by comparing the (001) projections of G and E in Fig. 11(c and e), it can be found that G is mainly increased along the [100] and [010] directions, while E is mainly increased along the [110] direction.

D. Intrinsic hardness of t-C4N Based on the elasticity results, it is known that t-C4N has outstanding polycrystalline elastic moduli and they all increased with the increase of pressure, which makes the prediction of its hardness more attractive and interesting. At present, there are two main models for calculating polycrystalline intrinsic hardness, the Chen's61 and Tian's[62] equations, which are given as follows:

$$H_{\mathrm{V}}(\mathrm{Chen}) = 2(k^2G)^{0.585} - 3 \qquad (14)$$

$$H_{\mathrm{V}}(\mathrm{Tian}) = 0.92k^{1.137}G^{0.708} \qquad (15)$$

where k = G/B is Pugh's modulus ratio.

The changes in pressure-induced polycrystalline hardness, anisotropic hardness and their 3D surface constructions of t-C4N are shown in Fig. 12. The detailed values of polycrystalline hardness HV(Chen's) and HV(Tian's), as well as minimum anisotropic hardness (Hmin) and maximum anisotropic hardness (Hmax) (dependent on crystal orientations, different from polycrystalline ones) calculated by energy–strain method, are listed in Table 3.

In Fig. 12, the pressure-induced Hmin and Hmax present opposite variations. With the increase of pressure, Hmax is increased, while Hmin is decreased. This difference leads to the increase in the anisotropy of hardness. The anisotropy increase can be intuitively observed in 3D surface constructions of hardness with different pressures. In 3D surface constructions, the blue areas represent lower hardness, and the yellow areas represent higher ones. Hmin can be obtained in both [100] and [010] orientations and Hmax can be obtained in the [110] orientation. The variation trends of the two calculated polycrystalline hardnesses are consistent with that of Hmin, which are gradually decreased with the increase of pressure. The pressure-induced reduction of polycrystalline hardness may be caused by abnormally increased anisotropy. The polycrystalline hardness models assume that the material is approximately isotropic, which will introduce a relatively larger error in the calculation results. The hardness values of t-C4N at 0 GPa obtained by the two polycrystalline hardness models are HV(Chen's) = 51.15 GPa and HV(Tian's) = 51.81 GPa, which indicate that t-C4N can be a potential superhard (HV >40 GPa[28]) material.

E. Pressure-induced toughness and brittleness of t-C4N

Based on the abnormal reduction in pressure-induced hardness, further studies were performed on the toughness and brittleness of t-C4N unit cells. The ductile–brittle results calculated using two universal criteria Cauchy pressure (C12–C44)63 and Pugh's modulus ratio (G/B)64 with different pressures (data in Table S8, ESI†) are shown in Fig. 13. In Fig. 13, the dashed line at C12–C44 = 0 in the horizontal direction indicates the position of critical zero Cauchy pressure as defined by Pettifor,63 and the dashed line at G/B = 0.571 in the vertical direction indicates the position of the critical Pugh's modulus ratio as defined by Pugh.64 When the pressures are 250 GPa, 300 GPa and 350 GPa, t-C4N meets both the conditions of C12–C44>0 and G/B<0.571, which correspond to the ductility and metallic bonding characteristics. When the pressures are 0 GPa and 50 GPa, t-C4N meets both the conditions of C12–C44 < 0 and G/B >0.571, which correspond to the brittleness and covalent bonding characteristics. However, when the pressures are 100 GPa, 150 Gpa and 200 Gpa, t-C4N is in the transition state from a brittle to ductile material. The positive Cauchy pressure indicates that it has a metallic bonding framework, and it is increased with the increase of pressure. The Pugh's modulus ratio is greater than 0.571, which indicates that it is brittle. The G/B ratio is decreased with the increase of pressure, which suggests there is a pressure-induced brittle-to-ductile transition of t-C4N. This law is consistent with the pressure-induced reduction in the calculations of polycrystalline hardness. They all reveal that t-C4N exhibits better plasticity and toughness at a high applied pressure.

The mechanism of pressure effect on the mechanical properties of t-C4N can be determined from electronic structure and chemical bond characteristics investigations. The Electron Localization Function (ELF) provides a semi-quantitative method for electronic structure analysis and assists in verifying chemical bond types,65 and the equation is as follows:

$$\mathrm{ELF} = 1/[1 + (D_{(\mathrm{r})}/Dh_{(\mathrm{r})})^2] \qquad (16)$$

where D(r) is the real electron density and Dh(r) corresponds to the uniform electron gas density.

The values of the ELF range is from 0 to 1. The upper limit ELF = 1 corresponds to perfect localization. The value ELF = 1/2 indicates the electron-gas-like pair probability. The value ELF = 0 indicates that electrons are completely delocalized or there is no electron.

When the pressures are 0 GPa and 350 GPa, the isosurfaces of ELF = 0.8 and ELF projections of the (110) planes in t-C4N are shown in Fig. 14, and the C and N atoms are located at 2c Wyckoff sites. In Fig. 14(a), when the pressure is 0 GPa, the isosurfaces in the t-C4N structure are yellow hook faces with ELF = 0.8, which indicate the locations of the electron localization regions. Here, the shapes of the electron accumulation regions between C atoms are spheroids, which reflect that the C–C bond shapes are spherical ones. The electron accumulation regions between C and N atoms are interlinked irregular areas. In Fig. 14(b), the blue regions in the (110) projections with ELF = 0 indicate that the electrons are completely delocalized or there is no electron. The red regions with ELF = 1 indicate perfect localization states. Therefore, the C–C bonds in t-C4N with spherical-like ELF isosurfaces and electron shared regions are non-polar covalent bonds. It can be seen that the bonds between C and N atoms are also covalent ones. There are electron pairs on both sides of the N atoms and their bonding interactions with other atoms are relatively weaker. In Fig. 14(c), when the pressure is increased to 350 GPa, there is no significant change in the C–C bond electron accumulation regions. The connected areas of electron accumulation regions around the N atoms are destroyed. In Fig. 14(d), the electron localization regions of the C–C bonds are elongated. The areas of electron accumulation regions on both sides of the N atoms are decreased and the metallic bond regions with ELF = 0.5 are increased. From the ELF isosurface changes under different pressures shown in Fig. S5 (ESI†), it is known that an increase in external pressure will lead to weakening of the covalent bond strength in t-C4N and then contribute to the enhancement of metallic characteristics. It also reveals the mechanism of its pressure-induced polycrystalline hardness decrease.

F. Ideal strength of t-C4N

The polycrystalline hardness is related to the anisotropy of the crystal structure. The intrinsic hardness can be obtained accurately by ideal tensile and shear calculations of different crystal faces in t-C4N. The tensile and shear stress–strain curves of t-C4N when the pressure is 0 GPa are shown in Fig. 15. Fig. 15(a) shows the ideal tensile stress–strain curves of the different crystal faces in t-C4N. T0 is the initial point of tensile calculation. T1 is the highest point of the tensile stress–strain curve, which corresponds to the ideal tensile strength. T2 is the tensile fracture point of the structure. Detailed data of the tensile strengths and critical strains are listed in Table 4. The ideal tensile strength of the (001) plane is the largest, which is 150.17 GPa. The ideal tensile strength of the (100) plane is slightly smaller than that of the (001) plane, which is 149.28 GPa. The critical strain of the (100) plane is the largest and it can reach 36.13%. The ideal strength of the (110) plane is 75.39 GPa, which is slightly higher than that (63.46 GPa) of the (111) plane. Therefore, the ideal tensile strength of the (111) plane is the smallest, which suggests that the (111) planes allow easy cleavage. It is similar to diamond, in which the (111) planes are also weak ones.[66] On this basis, the shear strength of the (111) plane along different crystal orientations was calculated and evaluated. Fig. 15(b) shows the ideal shear strength–strain curves. The detailed data of the shear strengths and critical strains are listed in Table 5. The smallest ideal shear strength can be obtained in the (111)[1%10] orientation, and its value is 67.98 GPa, which suggests that the theoretical hardness of t-C4N is 67.98 GPa (>40 GPa28). In addition, the strain softening of the stress–strain curves has a size effect and computational multiscale methods[67,68] can exactly deal with such problems.

The ELF projections of the (100), (010) and (001) planes in t-C4N with 1% and 16% tensile strains along the [001] orientation are shown in Fig. 16. In Fig. 16(a), when the tensile strain is 1%, the electron shared regions with ELF 4 0.8 between C and N atoms can be obviously observed in a red dashed line framework, which reveals that the bond type of C–N is covalent bonding. In Fig. 16(b), when the tensile strain is 16%, the electron shared regions with ELF = 0.8 between C and N atoms (located at 2c Wyckoff sites) change to electronic gas states regions with ELF = 0.2, which reveals that the atomic scale uniaxial tensile calculation is essentially a process of chemical bond tensile fracture. In addition, the electronic structural changes in the tensile process of the (100), (110) and (111) planes and in the shear process of the (111) plane along different orientations are shown in Fig. S6 and S7 (ESI†). They all exhibit chemical bond fracture in specific orientations and lead to cleavage and break of different crystal faces. Finally, the structures are transformed into disordered ones and then they are destroyed.

The tensile and shear calculations of t-C4N with high pressure were not considered in this work. In addition, the process of tensile and shear calculations under high pressure is much more complex and many factors need to be taken into account. Therefore, it is worth calculating in detail in an independent research study.

IV. Discussion

Due to the existence of anisotropy, the hardness of a single crystal diamond varies in the range from 60 GPa to 120 GPa, and its value depends on crystallized plane orientations.1 The hardness of single crystal t-C4N also indicates orientation dependence. When the pressure is 0 GPa, the maximum anisotropic hardness of single crystal t-C4N is about 81 GPa in the [110] orientation and the minimum one is about 29 GPa in the [100] orientation. Its theoretical hardness predicted via tensile and shear simulations is about 68 GPa in the $[1\bar{1}0]$ orientation of the (111) planes. The Vickers hardness calculated using a polycrystalline hardness model is about 51 GPa. This property is comparable to some known superhard materials. The theoretical hardness (lowest shear strength) of superhard BC3 (in a cubic diamond structure) is about 53 GPa.[27] The hardness of superhard B3N[5,29] c-BN30 and bct-BN31 is about 44 GPa, 66 GPa (polycrystalline) and 65 GPa (polycrystalline), respectively. Therefore, t-C4N can be promising superhard materials at 0 GPa, 1 atm or low pressure.

The mechanical properties of t-C4N and diamond are also compared under high pressures as shown in Fig. 17 (data in TableS9, ESI†).With the increase of pressure, the Young's modulus, shear modulus, bulk modulus and Poisson's ratio of diamond and t-C4N are increased, while their hardness and Pugh's ratios are decreased. Their bulk moduli have similar values and variation tendency under pressure. Thus, the change in Young's modulus or shear modulus determines that of the other one. The hardness decreasing rate of diamond is slower than that of t-C4N. From 0 GPa to 350 GPa, the Pugh's ratios of diamond are all larger than 0.571, which indicates the brittleness and covalent bonding characteristics. That of t-C4N is smaller than 0.571 when the pressure is 250 GPa (and higher ones), which reveals a pressure-induced brittle–ductile transition. The higher Poisson's ratio of t-C4N indicates its better lateral deformation ability than that of diamond under different pressures. Although the theoretical hardness of t-C4N is lower than that of diamond and plagued by pressure-induced polycrystalline hardness reduction, it still has the potential to be used as an industrial superhard material.

V. Conclusions

A novel t-C4N with a 3D structure is predicted successfully by CALYPSO and first principles calculations. There is no imaginary
frequency in the phonon spectrum, which proves that t-C4N is thermodynamically stable. t-C4N is equipped with excellent elastic properties. The B, G and E moduli are all gradually increased with the increase in pressure. When the pressure is 0 GPa, the polycrystalline hardness values of t-C4N are HV(Chen's) = 51.15 GPa and HV(Tian's) = 51.81 GPa, respectively. The maximum Hmax and minimum Hmin of its anisotropic hardness are 81.12 GPa and 29.45 GPa, respectively. With the increase of pressure, Hmax is increased and Hmin is gradually decreased. Polycrystalline hardness is decreased with the increase of pressure, which may be caused by the increase of pressure-induced anisotropy. For the anisotropy of the t-C4N crystal structure, the atomic-scale tensile and shear calculations for different crystal planes are performed to determine a more accurate theoretical hardness. The smallest ideal strength (63.46 GPa) can be obtained in the (111) plane, which indicates that the (111) planes allow easy cleavage. The smallest ideal shear strength (67.98 GPa) can be obtained in the (111)[1%10] orientation. This suggests the theoretical hardness of t-C4N is 67.98 GPa.

Data availability

All data generated or analyzed during this study are included in this published article and the original data is available on request.

Conflicts of interest

There are no conflicts to declare.

Acknowledgements

The authors would like to express their gratitude for projects supported by the National Natural Science Foundation of China(No. 51771167) and the EU H2020 Marie Skłodowska-Curie project "i-Weld" (No. 823786).

References

1 T. Irifune, A. Kurio, S. Sakamoto, T. Inoue and H. Sumiya, Nature, 2003, 421, 599–600, DOI: 10.1038/421599b.
2 H. Abbasian and A. Rochefort, Phys. Chem. Chem. Phys.,2021, 23, 22014–22021.
3 Y. X. Yu, J. Mater. Chem. A, 2013, 1, 13559–13566.
4 J. Kang, J. Li, F. Wu, S. S. Li and J. B. Xia, J. Phys. Chem. C, 2011, 115, 20466–20470.
5 J. Kim, M. S. Choi, K. H. Shin, M. Kota, Y. Kang, S. Lee, J. Y. Lee and H. S. Park, Adv. Mater., 2019, 31, 1–20.
6 R. Gholizadeh and Y. X. Yu, J. Phys. Chem. C, 2014, 118, 28274–28282.
7 Z. Li, C. Bommier, Z. Sen Chong, Z. Jian, T. W. Surta, X. Wang, Z. Xing, J. C. Neuefeind, W. F. Stickle, M. Dolgos, P. A. Greaney and X. Ji, Adv. Energy Mater., 2017, 7, 1–10.
8 J. Xia, L. Chai, T. Tian, H. Li, F. Hao, Y. Cui, Y. Wang, M. Li and Y. Zhu, Powder Technol., 2020, 373, 488–496.
9 A. Bafekry, C. Stampfl, M. Ghergherehchi and S. Farjami Shayesteh, Carbon, 2020, 157, 371–384.
10 D. Wang, Y. Bao, T. Wu, S. Gan, D. Han and L. Niu, Carbon, 2018, 134, 22–28.

11 J. Du and X. Li, J. Alloys Compd., 2020, 815, 152324.
12 Y. Li, C. Mo, J. Li and D. Yu, J. Energy Chem., 2020, 49, 243–247.
13 M. Faisal, M. Jalalah, F. A. Harraz, A. M. El-Toni, A. Khan and M. S. Al-Assiri, Ceram. Int., 2020, 46, 22090–22101.
14 E. C. Franklin, J. Am. Chem. Soc., 1922, 44, 486–509.
15 S. Cao and J. Yu, J. Phys. Chem. Lett., 2014, 5, 2101–2107.
16 M. Wu, Q. Wang, Q. Sun and P. Jena, J. Phys. Chem. C, 2013, 117, 6055–6059.
17 Z. Zhao, Y. Sun and F. Dong, Nanoscale, 2015, 7, 15–37.
18 Z. Liang, B. Xu, H. Xiang, Y. Xia, J. Yin and Z. Liu, RSC Adv., 2016, 6, 54027–54031.
19 S. Guan, Y. Cheng, C. Liu, J. Han, Y. Lu, S. A. Yang and Y. Yao, Appl. Phys. Lett., 2015, 107, 231904.
20 B. Mortazavi, Carbon, 2017, 118, 25–34.
21 Y. Yin, H. Chen and Q. Yuan, Chem. Phys. Lett., 2021, 768, 138390.
22 L. Li, X. Kong, O. Leenaerts, X. Chen, B. Sanyal and F. M. Peeters, Carbon, 2017, 118, 285–290.
23 R. Zhang, W. Jian, Z. Di Yang and F. Q. Bai, Chinese Chem. Lett., 2020, 31, 2319–2324.
24 C. Yang, Z. Di Yang, H. Dong, N. Sun, Y. Lu, F. M. Zhang and G. Zhang, ACS Energy Lett., 2019, 4, 2251–2258.
25 Y. Wang, J. Lv, L. Zhu and Y. Ma, Phys. Rev. B: Condens. Matter Mater. Phys, 2010, 82, 1–8.
26 C. Pu, D. Zhou, Y. Li, H. Liu, Z. Chen, Y. Wang and Y. Ma, J. Phys. Chem. C, 2017, 121, 2669–2674.
27 M. Zhang, H. Liu, Q. Li, B. Gao, Y. Wang, H. Li, C. Chen and Y. Ma, Phys. Rev. Lett., 2015, 114, 1–5.
28 M. Zhang, M. Lu, Y. Du, L. Gao, C. Lu and H. Liu, J. Chem. Phys., 2014, 140, 174505.
29 Y. Li, J. Hao, H. Liu, S. Lu and J. S. Tse, Phys. Rev. Lett., 2015, 115, 1–5.
30 P. B. Mirkarimi, K. F. McCarty and D. L. Medlin, Mater. Sci. Eng. R Reports, 1997, 21, 47–100.
31 B. Wen, J. Zhao, R. Melnik and Y. Tian, Phys. Chem. Chem. Phys., 2011, 13, 14565–14570.
32 L. Zhang, Y. Wang, J. Lv and Y. Ma, Nat. Rev. Mater., 2017, 2, 17005.
33 Z. Zhao, B. Xu and Y. Tian, Annu. Rev. Mater. Res., 2016, 46, 383–406.
34 C. J. Pickard, A. Salamat, M. J. Bojdys, R. J. Needs and P. F. McMillan, Phys. Rev. B, 2016, 94, 1–10.
35 S. Lu, Y. Wang, H. Liu, M. S. Miao and Y. Ma, Nat. Commun., 2014, 5, 3–8.
36 B. Gao, P. Gao, S. Lu, J. Lv, Y. Wang and Y. Ma, Sci. Bull., 2019, 64, 301–309.
37 K. Yin, P. Gao, X. Shao, B. Gao, H. Liu, J. Lv, J. S. Tse, Y. Wang and Y. Ma, npj Comput. Mater., 2020, 6, 1–10.
38 G. Kresse and J. Furthmuller, Phys. Rev. B, 1996, 54, 11169–11186.
39 P. E. Blo¨chl, Phys. Rev. B, 1994, 50, 17953–17979.
40 J. P. Perdew, K. Burke and M. Ernzerhof, Phys. Rev. Lett., 1996, 77, 3865–3868.
41 A. van de Walle and G. Ceder, Phys. Rev. B: Condens. Matter Mater. Phys., 1999, 59, 14992–15001.
42 K. Parlinski, Z. Q. Li and Y. Kawazoe, Phys. Rev. Lett., 1997, 78, 4063–4066.
43 L. Chaput, A. Togo, I. Tanaka and G. Hug, Phys. Rev. B: Condens. Matter Mater. Phys., 2011, 84, 1–6.
44 D. Conne´table and O. Thomas, Phys. Rev. B: Condens. Matter Mater. Phys., 2009, 79, 1–9.
45 H. M. Tu¨tu¨ncu¨, S. Bagci and G. P. Srivastava, J. Phys.: Condens. Matter, 2007, 19, 156207.
46 W. Luo, D. Roundy, M. L. Cohen and J. W. Morris, Phys. Rev. B: Condens. Matter Mater. Phys., 2002, 66, 1–7.
47 D. Roundy, C. R. Krenn, M. L. Cohen and J. W. Morris, Phys. Rev. Lett., 1999, 82, 2713–2716.
48 Z. Shi, A. Kutana and B. I. Yakobson, J. Phys. Chem. Lett., 2015, 6, 106–112.
49 Y. Ding and Y. Wang, Nanoscale Res. Lett., 2015, 10, 1–11.
50 C. Pu, D.i Zhou, Y. Li, H. Liu, Z. Chen, Y. Wang and Y. Ma, J. Phys. Chem. C, 2017, 121, 2669–2674.
51 Y. X. Yu, Appl. Surf. Sci., 2021, 546, 149062.
52 J. Wu, J. H. Li and Y. X. Yu, Phys. Chem. Chem. Phys., 2020, 22, 7633–7642.
53 J. W. Yang and L. An, Solid State Commun., 2020, 316–317, 13–19.
54 J. A. D. Matthew, Acta Crystallogr. Sect. A, 1970, 26, 702.
55 W. Voigt, Lehrb. Krist., 1966, 7, 560–798.
56 A. Reuss, ZAMM – J. Appl. Math. Mech./Z. Angew. Math. Mech., 1929, 9, 49–58.

57 R. Hill, Proc. Phys. Soc. Sect. A, 1952, 65, 349–354.
58 P. Ravindran, L. Fast, P. A. Korzhavyi, B. Johansson, J. Wills and O. Eriksson, J. Appl. Phys., 1998, 84, 4891–4904.
59 R. Gaillac, P. Pullumbi and F. X. Coudert, J. Phys.: Condens. Matter, 2016, 28, 275201.
60 M. Liao, Y. Liu, L. Min, Z. Lai, T. Han, D. Yang and J. Zhu, Intermetallics, 2018, 101, 152–164.
61 X. Q. Chen, H. Niu, D. Li and Y. Li, Intermetallics, 2011, 19, 1275–1281.
62 Y. Tian, B. Xu and Z. Zhao, Int. J. Refract. Met. Hard Mater., 2012, 33, 93–106.
63 D. G. Pettifor, Mater. Sci. Technol., 1992, 8, 345–349.
64 S. F. Pugh, London, Edinburgh, Dublin Philos. Mag. J. Sci., 1954, 45,
823–843.
65 A. D. Becke and K. E. Edgecombe, J. Chem. Phys., 1990, 92, 5397–5403.
66 D. Roundy and M. L. Cohen, Phys. Rev. B: Condens. Matter Mater. Phys., 2001, 64, 2–4.
67 H. Talebi, M. Silani, S. Bordas, P. Kerfriden and T. Rabczuk, Comput. Mech., 2014, 53, 1047–1071.
68 H. Talebi, M. Silani and T. Rabczuk, Adv. Eng. Softw., 2015, 80, 82–92.

Table 1 Elastic constants of t-C_4N under different pressures

Pressure (GPa)	C_{11} (GPa)	C_{12} (GPa)	C_{13} (GPa)	C_{33} (GPa)	C_{44} (GPa)	C_{66} (GPa)
0	725.11	295.19	136.03	1317.53	394.67	418.02
50	871.35	412.83	225.47	1595.61	444.61	529.05
100	1000.68	529.65	299.52	1840.95	481.67	593.71
150	1112.07	636.01	372.47	2062.68	508.01	651.48
200	1213.19	735.62	443.28	2281.83	528.97	722.52
250	1307.41	828.96	512.29	2491.46	547.97	813.47
300	1394.89	917.47	584.78	2690.43	563.43	937.26
350	1459.27	987.99	643.72	2828.78	558.62	1034.32

Table 2 Calculated *B*, *G* and *E* *via* the Voigt–Reuss–Hill method

(GPa)	B_V	B_R	B_H	G_V	G_R	G_H	E_V	E_R	E_H
0	433.6	420.2	426.9	388.2	354.6	371.4	896.9	830.2	863.7
50	562.9	544.9	553.9	448.6	400.5	424.6	1063.4	965.1	1014.5
100	677.7	657.1	667.4	492.3	430.1	461.2	1189.0	1059.3	1124.6
150	783.2	759.3	771.2	527.2	451.1	489.1	1291.8	1129.5	1211.3
200	883.6	855.4	869.5	561.8	469.1	515.4	1390.7	1189.6	1291.1
250	979.3	946.3	962.8	598.7	486.2	542.5	1492.1	1245.3	1370.1
300	1072.7	1034.2	1053.5	639.1	501.6	570.3	1599.5	1295.4	1449.4
350	1144.2	1102.1	1123.1	661.8	504.2	582.9	1664.4	1312.4	1490.9

Table 3 Pressure-induced polycrystalline hardness and anisotropic hardness H_{min}/H_{max} (GPa)

Pressure	H_V(Chen's)	H_V(Tian's)	H_{min}	H_{max}
0	51.15	51.81	29.45	81.12
50	47.49	49.32	25.45	84.29
100	43.95	46.49	22.13	86.23
150	40.95	43.96	19.41	88.15
200	38.87	42.25	17.24	93.01
250	37.66	41.35	15.55	101.16
300	36.95	40.93	14.09	113.59
350	35.53	39.64	12.83	122.41

Table 4 Atomic-scale tensile result of different crystal faces in t-C_4N

	Ideal strength (GPa)	Critical strain (%)
⟨001⟩	150.17	16.09
⟨100⟩	149.28	36.13
⟨110⟩	75.39	22.02
⟨111⟩	63.46	11.57

Table 5 Atomic-scale shear results of the (111) crystal face in different orientations

	Shear strength (GPa)	Critical strain (%)
$(111)[0\bar{1}1]$	74.89Z	23.13
$(111)[1\bar{1}0]$	67.98	34.52
$(111)[\bar{1}\bar{1}2]$	141.03	29.91
$(111)[11\bar{2}]$	76.96	27.62
$(111)[\bar{1}01]$	76.38	23.13
$(111)[\bar{1}10]$	70.53	39.23

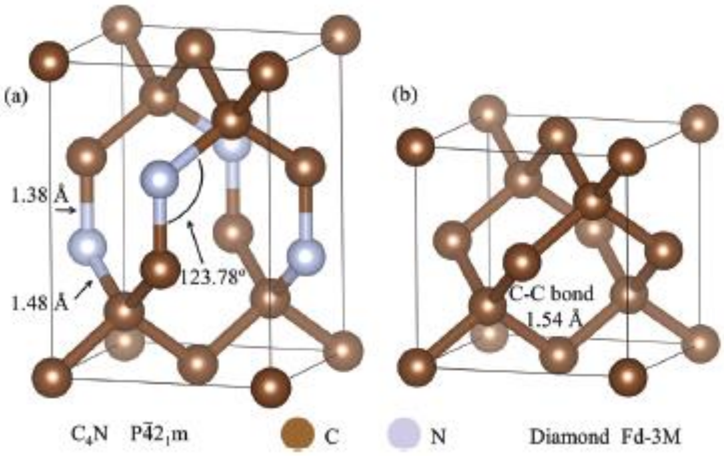

Fig. 1 Schematic diagrams of (a) t-C4N and (b) the diamond unit cell.

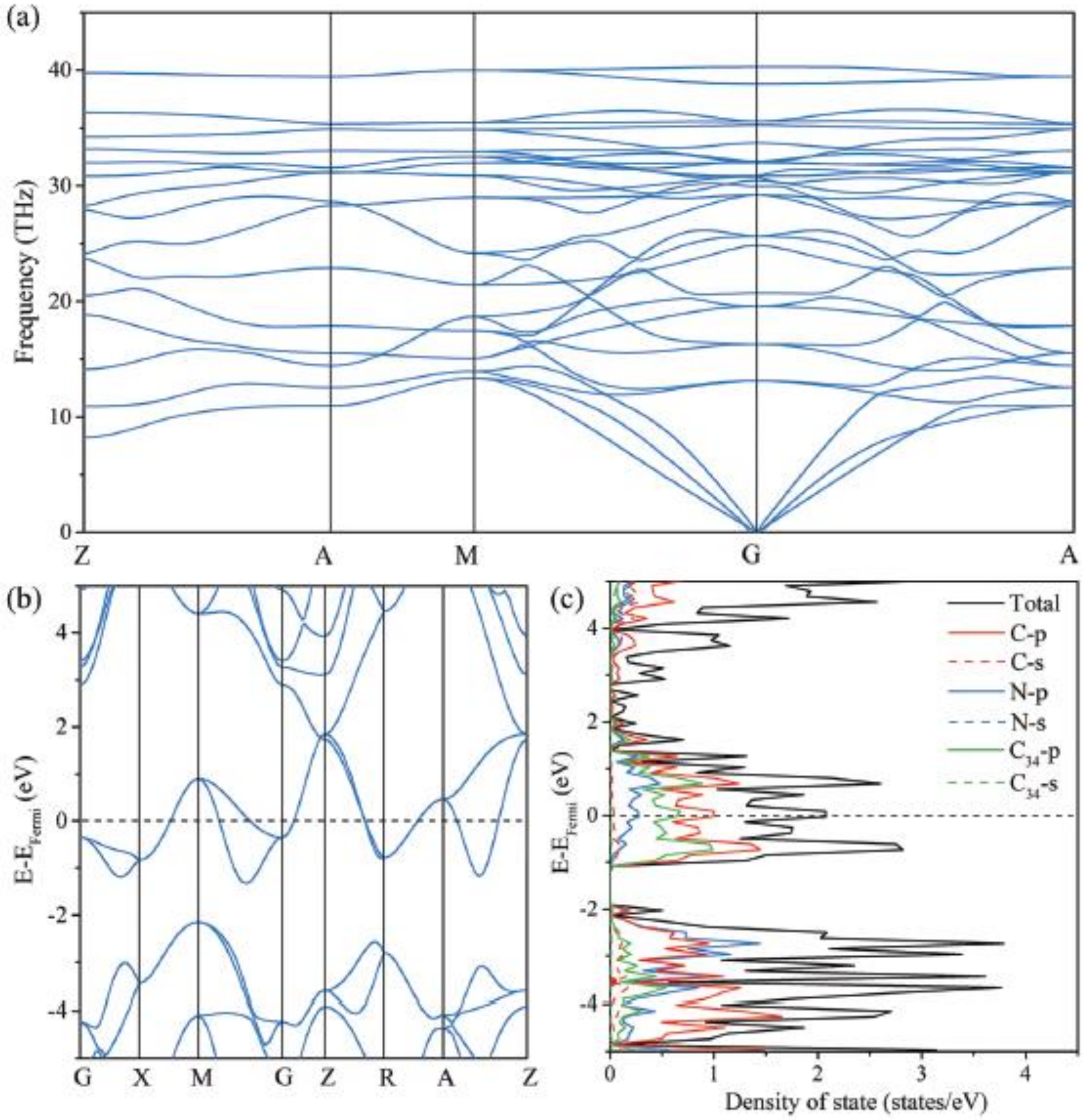

Fig. 2 Stability and bulk properties of t-C4N. (a) Phonon spectrum, (b) band structure and (c) TDOS and PDOS.

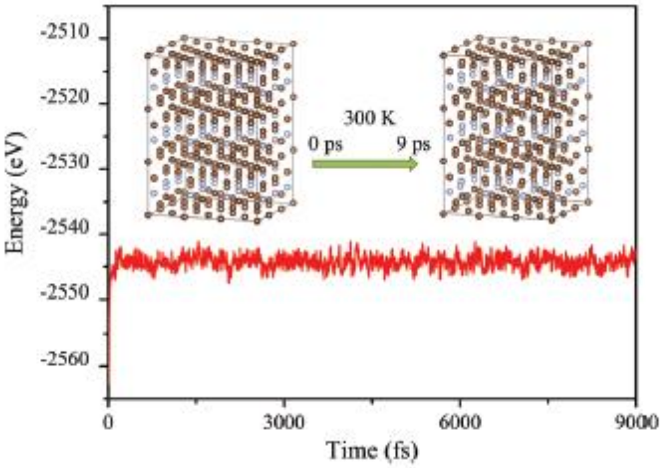

Fig. 3 Relationship between total energy and simulation time of t-C4N

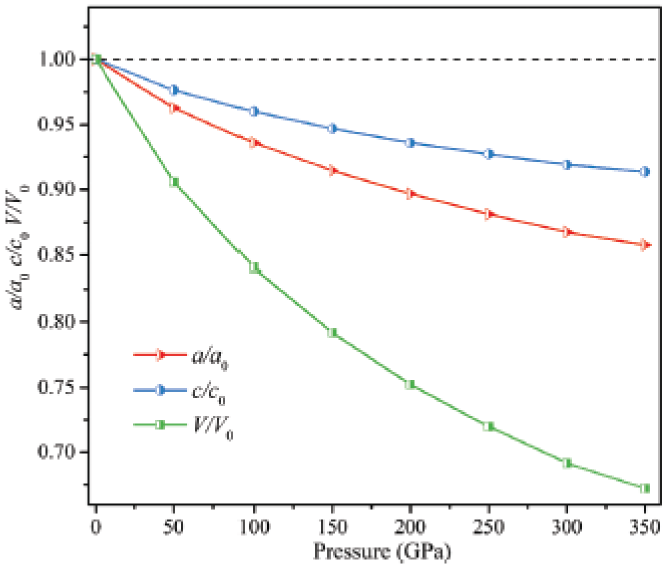

Fig. 4 Pressure-induced a/a0, c/c0 and V/V0 ratios of t-C4N.

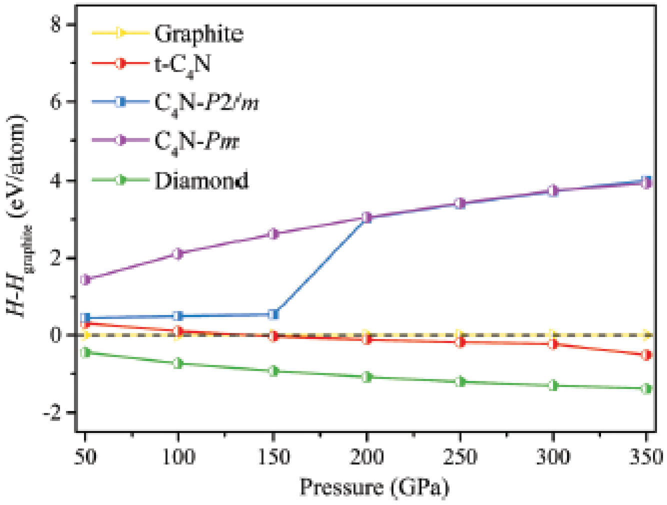

Fig. 5 Pressure-induced enthalpy changes of t-C4N, diamond and 2D C4N compared to graphite.

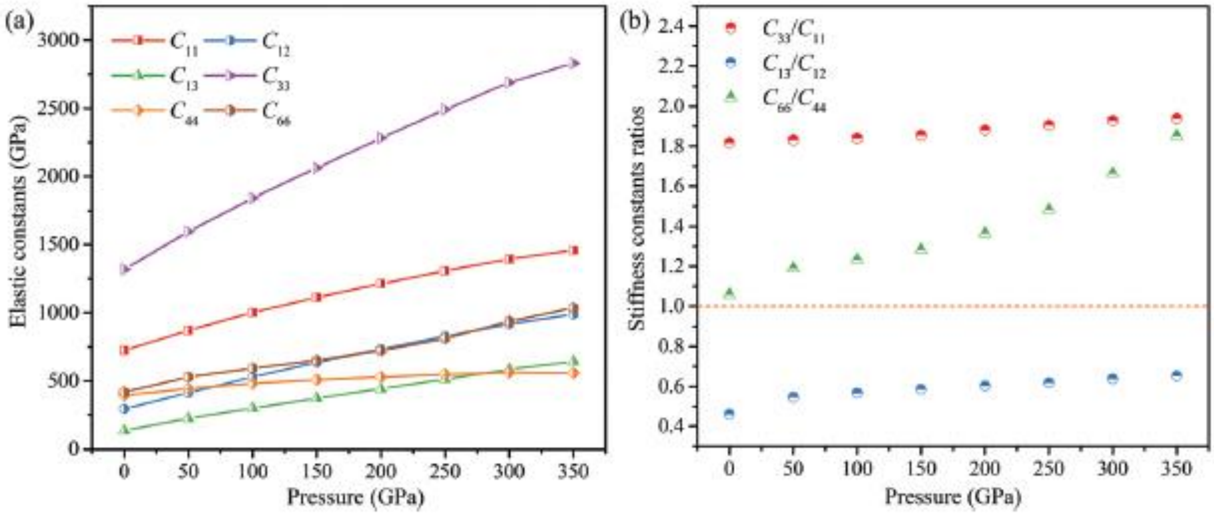

Fig. 6 Pressure-induced elastic/stiffness constants of t-C4N. (a) Elastic constant–pressure curves and (b) stiffness constant–pressure curves

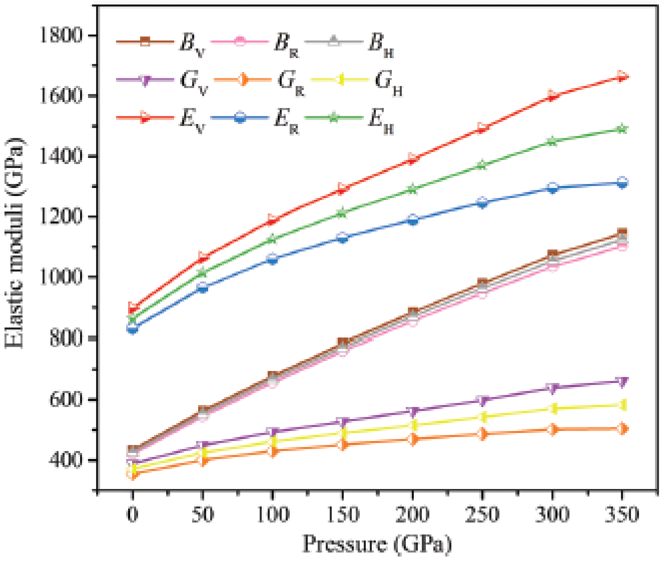

Fig. 7 Pressure-induced bulk modulus B, shear modulus G and Young’ s modulus E curves.

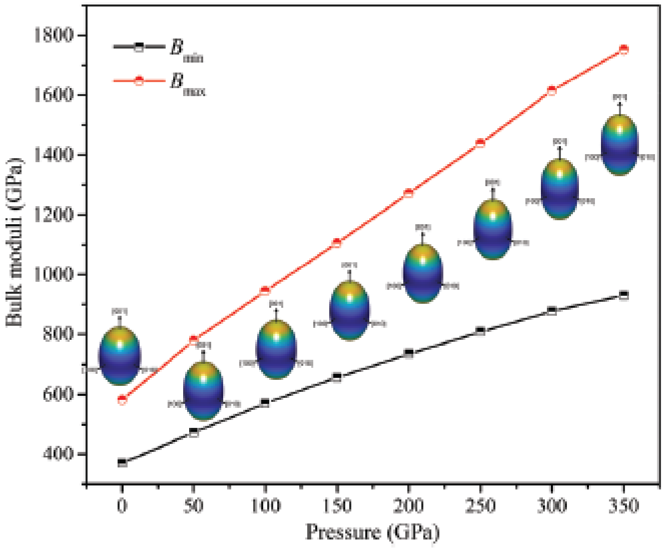

Fig. 8 Changes of Bmin, Bmax and 3D surface constructions of pressure induced bulk moduli.

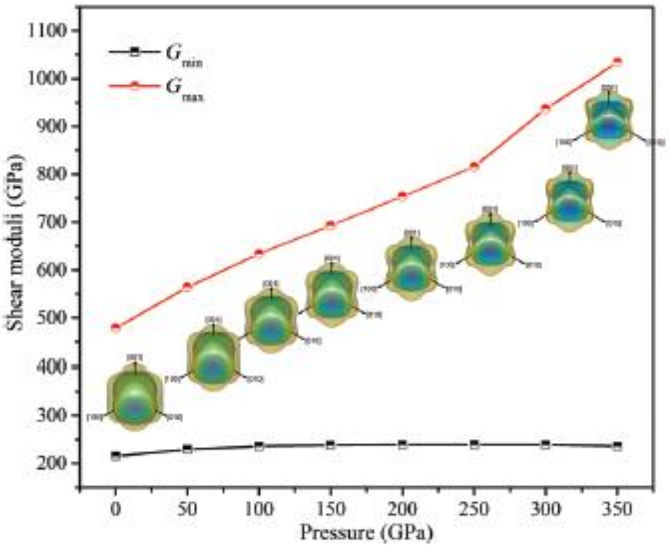

Fig. 9 Changes in the Gmin, Gmax and 3D surface constructions of pressure-induced shear moduli.

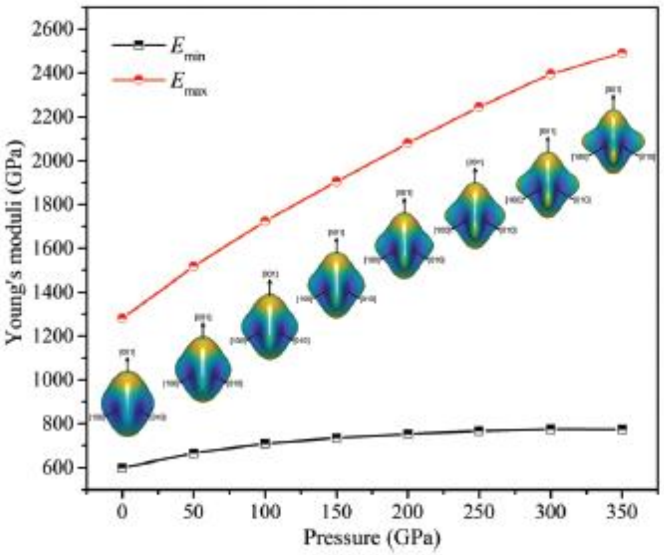

Fig. 10 Changes of Emin, Emax and 3D surface constructions of pressure-induced Young' s moduli.

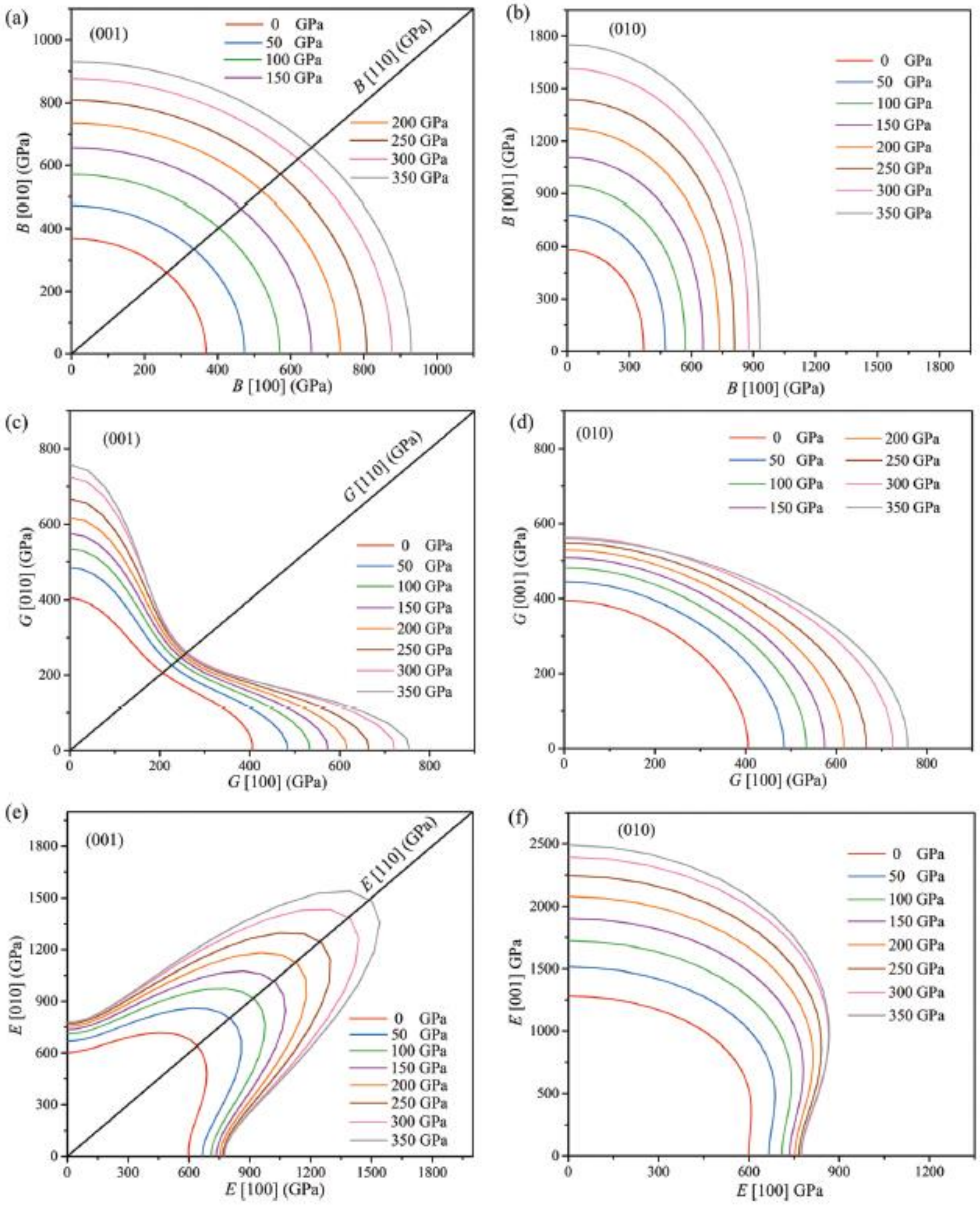

Fig. 11 (001) and (010) projections of pressure-induced elastic moduli B, G and E (the entire projections can be obtained by symmetry operation). (a) (001) projections of B, (b) (010) projections of B, (c) (001) projections of G, (d) (010) projections of G, (e) (001) projections of E, and (f) (010) projections of E.

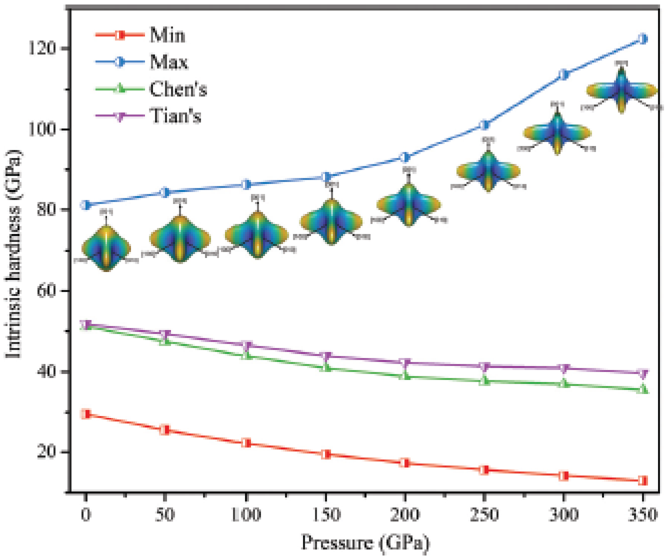

Fig. 12 Changes of pressure-induced intrinsic hardness and 3D surface constructions.

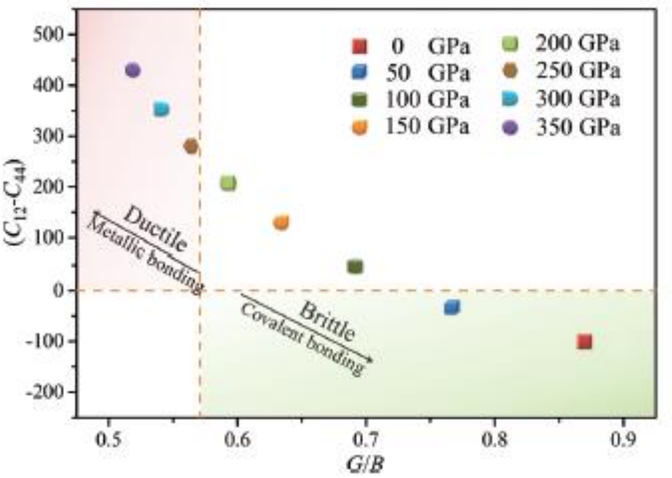

Fig. 13 The effects of pressure on the ductility and brittleness of t-C4N calculated via universal criterion Cauchy pressure C12–C44 and Pugh’s modulus ratio G/B.

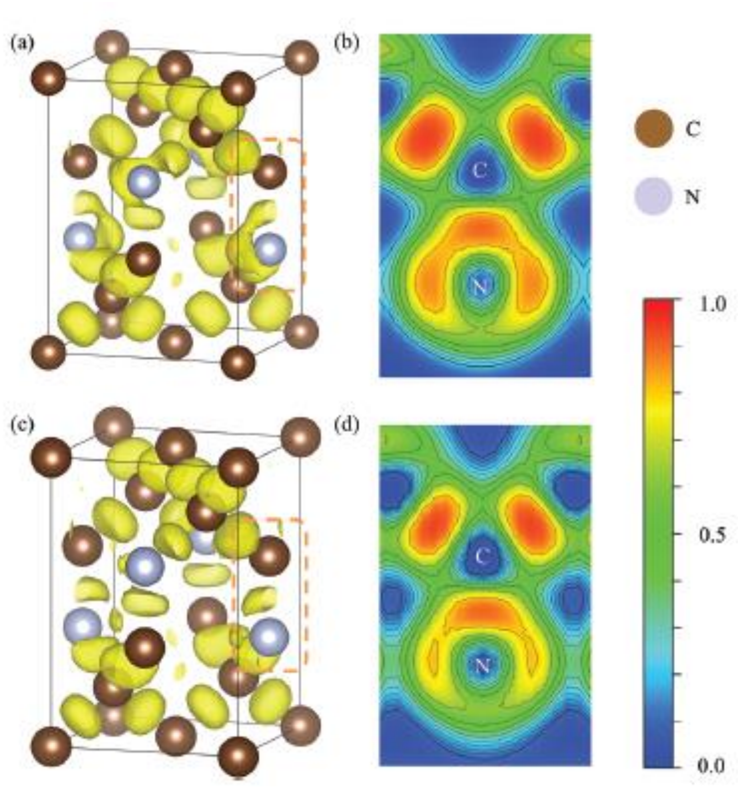

Fig. 14 The effects of pressure on the electronic structure and chemical ond characteristics of t-C4N. (a) ELF isosurface (ELF 0.8) and (b) projections of (110) planes under 0 GPa. (c) ELF isosurface (ELF 0.8) and (d) projections of (110) planes under 350 GPa.

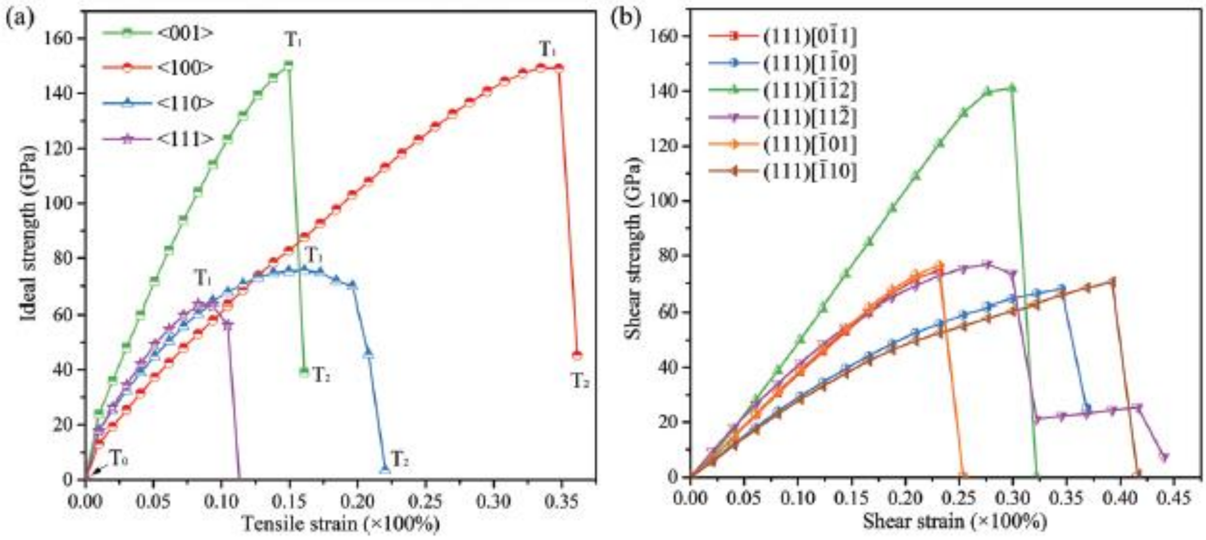

Fig. 15 Stress–strain curves of t-C4N when the pressure is 0 GPa. (a) Tensile stress–strain curves of the (001), (100), (110) and (111) crystal faces. (b) Shear stress–strain curves of the (111) face with different shear orientations.

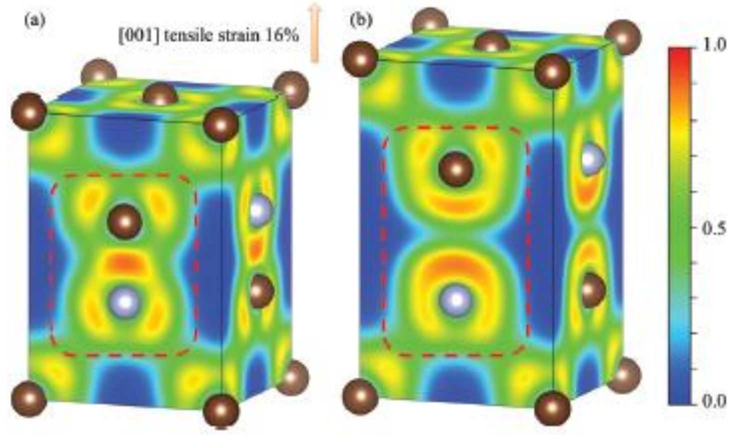

Fig. 16 Schematic diagrams of ELF projections in the (100), (010) and (001) planes of t-C4N with (a) 1% and (b) 16% tensile strain at the [001] orientation.